Resolving Charge Transfer Mechanisms in Molecular Tunnel Junctions using Dynamic Charge Transfer and Static Current-Voltage Measurements

Liang Cao[1, ‡], Ziyu Zhang[2, ‡], Damien Thompson[3], Dong-Chen Qi[4*], Christian A. Nijhuis[5*]*

[1]Anhui Key Laboratory of Low-energy Quantum Materials and Devices, High Magnetic Field Laboratory, HFIPS, Chinese Academy of Sciences, Hefei 230031, P. R. China

[2]Department of Chemistry, National University of Singapore, 3 Science Drive, Singapore 117543, Singapore.

[3]Department of Physics, Bernal Institute, University of Limerick, Limerick V94 T9PX, Ireland.

[4]Centre for Materials Science, School of Chemistry and Physics, Queensland University of Technology, Brisbane, Queensland 4001, Australia.

[5]Hybrid Materials for Opto-Electronics Group, Department of Molecules and Materials, MESA+ Institute for Nanotechnology and Center for Brain-Inspired Nano Systems, Faculty of Science and Technology, University of Twente, P.O. Box 217, 7500 AE Enschede, The Netherlands.

*Authors to whom correspondence should be addressed: damien.thompson@ul.ie, dongchen.qi@qut.edu.au, and c.a.nijhuis@utwente.nl

‡ These authors contributed equally

S1. Fabrication of template-stripped metal surfaces and formation of self-assembled monolayers (SAMs).

Template-stripped (TS) metal surfaces were made following established procedures.[1] 400 nm Ag and 200 nm Au were deposited on silicon wafers using a thermal evaporator (Sky Technology Development DHN-400). 40 nm Pt was deposited using an electron beam evaporator (Denton Vacuum Explorer, NJ USA). Glass slides were cleaned with piranha solution and glued to the metal surface using EPOTEK 353ND thermal glue. The samples were heated to 80 °C and for 3 h for the glue to cure, after which the glass–metal surfaces were removed from the silicon wafers. The freshly prepared Ag^{TS}, Au^{TS} and Pt^{TS} surfaces were immersed in a solution of the SAM precursor, *i.e.*, $SH-CH_2-OPE_nFc$ (n = 1-3) in THF/ethanol (1:5), under an atmosphere of argon for 8 h at room temperature to allow the SAMs to form. Then, the samples were rinsed with THF and ethanol immediately after being taken out of the solutions, and then dried in a gentle flow of N_2 gas.

S2. Photoemission spectroscopy

The photoemission spectroscopy (PES), near-edge X-ray absorption fine structure (NEXAFS) and resonant photoemission spectroscopy (RPES) were conducted at the Soft X-ray Spectroscopy beamline of the Australian Synchrotron. The equipment and measurement setup were described in our previous work.[2] In this study, we recorded high resolution scans for C $1s$, S $2p$ and Fe $2p$ spectra for all the SAMs and Ag $3d$, Au $4f$ and Pt $4f$ spectra for the corresponding metal surfaces. For each region we measured the signals at take-off angles θ of 90º (normal emission, NE) and 20º (grazing emission, GE). The high resolution PES spectra for the SAM on Au, Pt and Ag are shown in Figure S1-S4, the respective results for those SAMs on Au are also given in ref[3]. We estimated the SAM film thickness d_{SAM} using the signals intensities of S $2p$ spectra at NE and GE.[3] The results are summarized in Table S1. Figure S2 shows that two C $1s$ signals are present for each SAM: C_1 (~284.8 eV, green line) represents the sp^2 carbon atoms in the OPE, while C_2 (~285.2 eV, blue line) are the sp^2 carbon atoms in the cyclopentadienyl (Cp) groups.[4] The relative intensity of C_1 to C_2 increases as n, supporting our assignment.
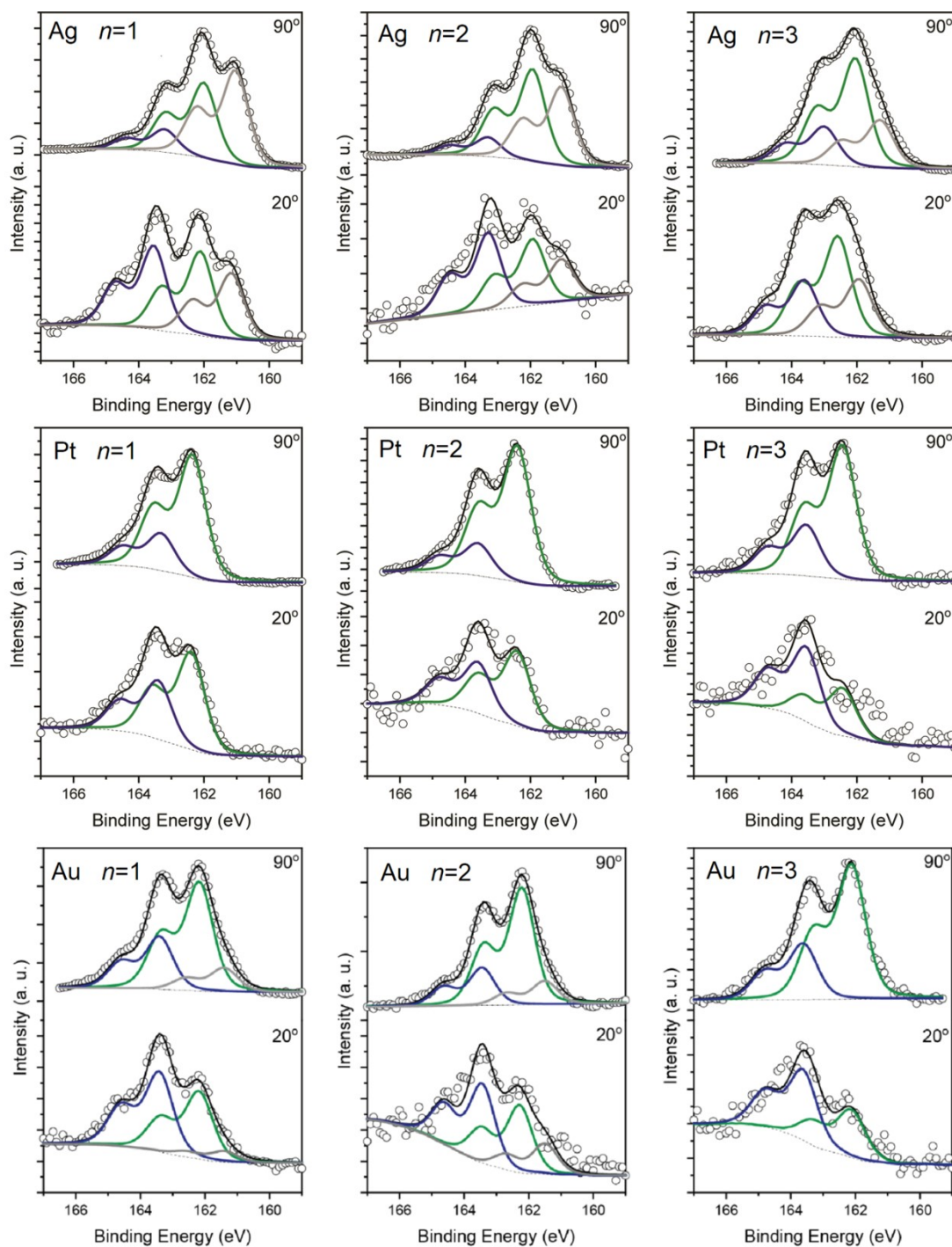
Figure S1. S $2p$ spectra of the SAMs of Ag/S-CH$_2$-OPE$_n$Fc, Pt/S-CH$_2$-OPE$_n$Fc and Au/S-CH$_2$-OPE$_n$Fc (n = 1−3) collected using a photon energy of 350 eV. Each spectrum can be well-fitted using two or three doublets, where each doublet contains S $2p_{3/2}$ and S $2p_{1/2}$ features with a ratio of 2 ($2p_{3/2}$):1 ($2p_{1/2}$) and a spin-orbit coupling energy of ~1.2 eV.[5] The grey solid line represents the S$_0$ peak doublet, the green solid line represents the S$_1$ peak doublet and the blue solid line represents the S$_2$ doublet. Only the peak intensity of S$_2$ increases substantially with a decrease of emission angle θ indicating that physisorbed material is present on the SAM.
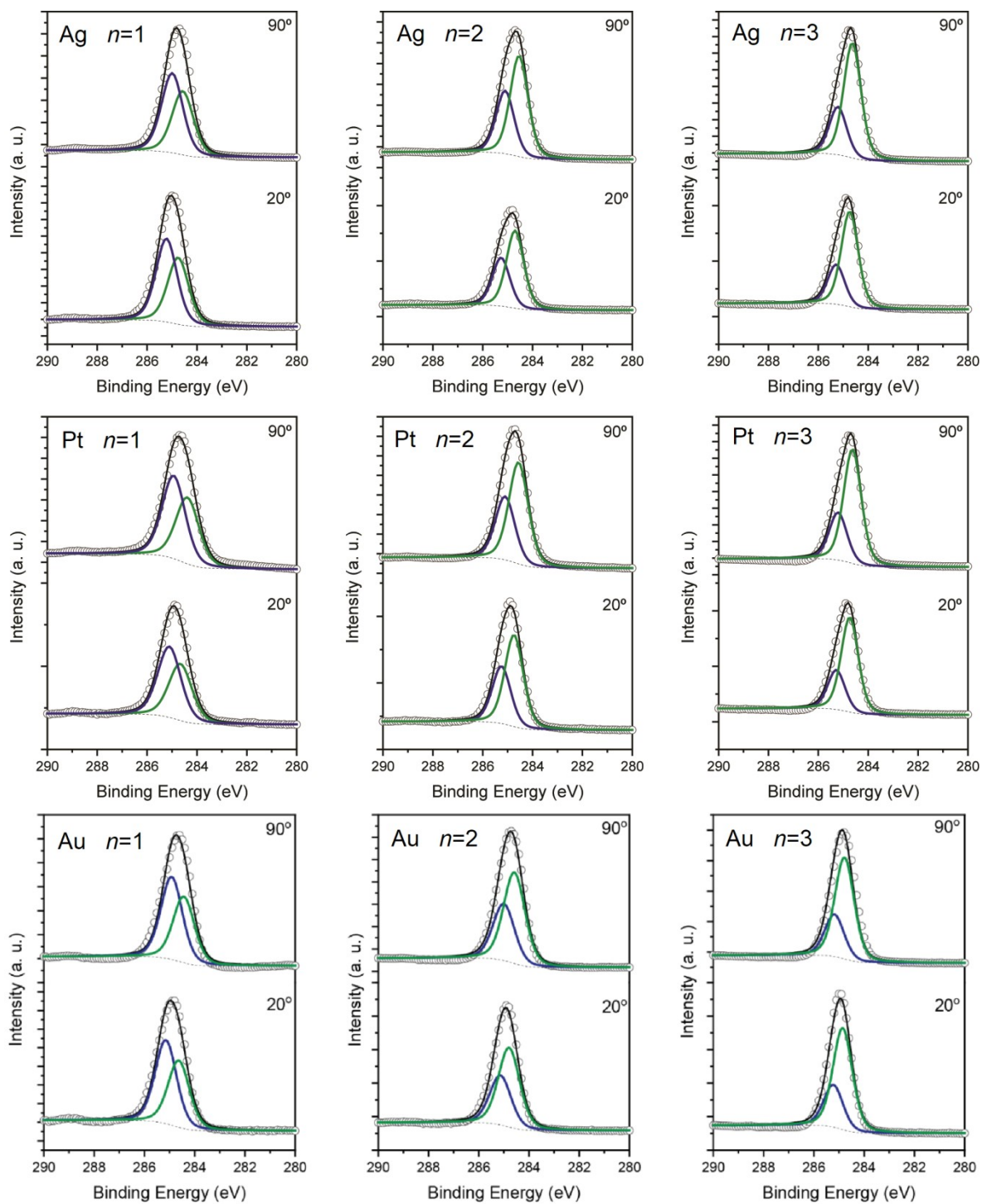
Figure S2. C 1s spectra of the SAMs of Ag/S-CH$_2$-OPE$_n$Fc, Pt/S-CH$_2$-OPE$_n$Fc and Au/S-CH$_2$-OPE$_n$Fc (n = 1−3) collected by photon energy of 350 eV. Two C 1s signals are present for each SAM: C$_1$ (~284.8 eV, green line) represents the sp^2 carbon atoms in the OPE, while C$_2$ (~285.2 eV, blue line) are the sp^2 carbon atoms in the cyclopentadienyl (Cp) groups.[4] The relative intensity of C$_1$ to C$_2$ increases with n, supporting our peak assignment.
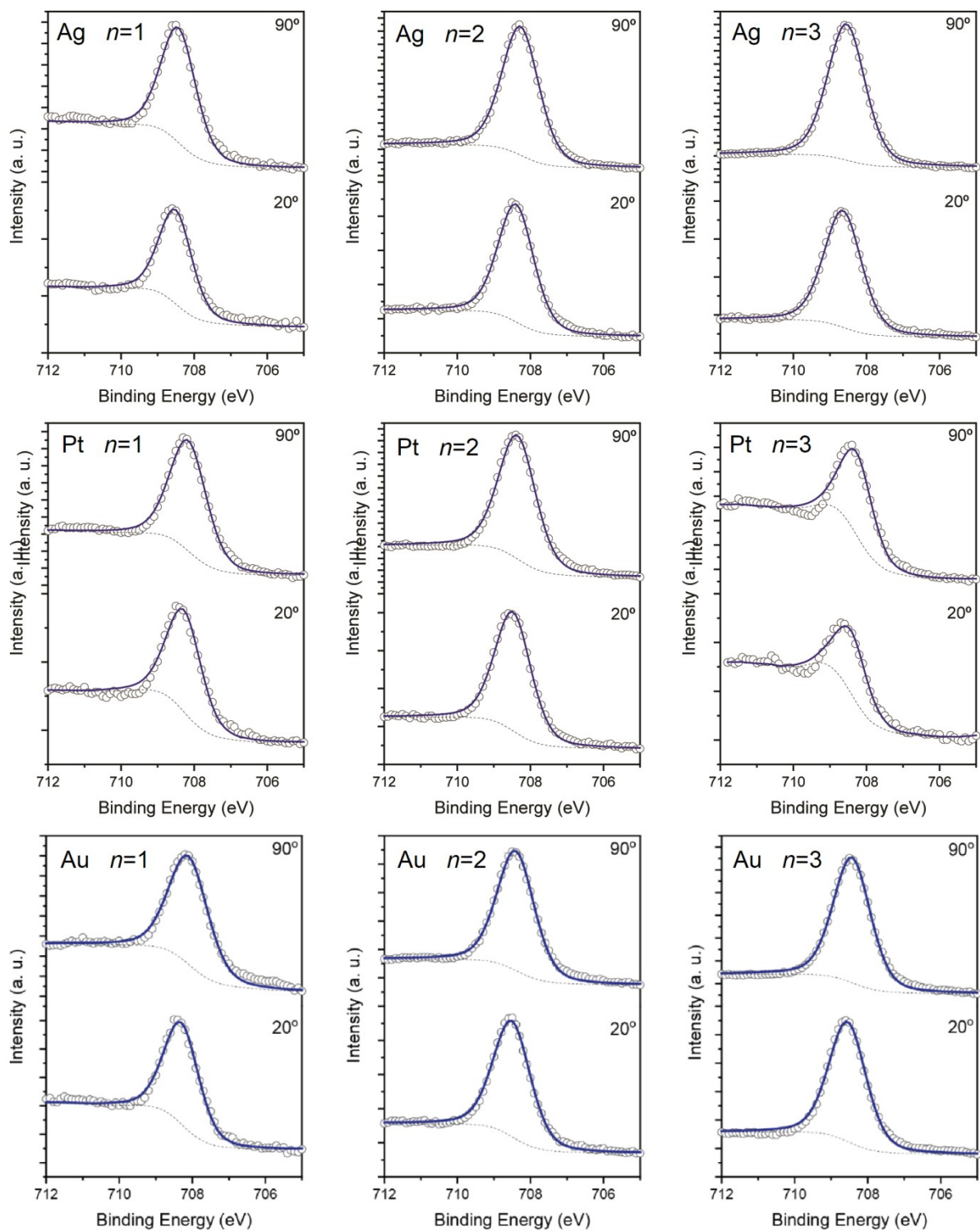
Figure S3. Fe $2p_{3/2}$ spectra of SAMs Ag/S-CH$_2$-OPE$_n$Fc, Pt/S-CH$_2$-OPE$_n$Fc and Au/S-CH$_2$-OPE$_n$Fc ($n = 1{-}3$) collected using photon energy of 850 eV. The Fe $2p_{3/2}$ spectra for n=3 on Pt are less intense than those for n=1 and n=2; these differences in intensities do not affect our conclusions and main observations since they are based on the ratios of the integrated intensities of the resonant valence band spectra.
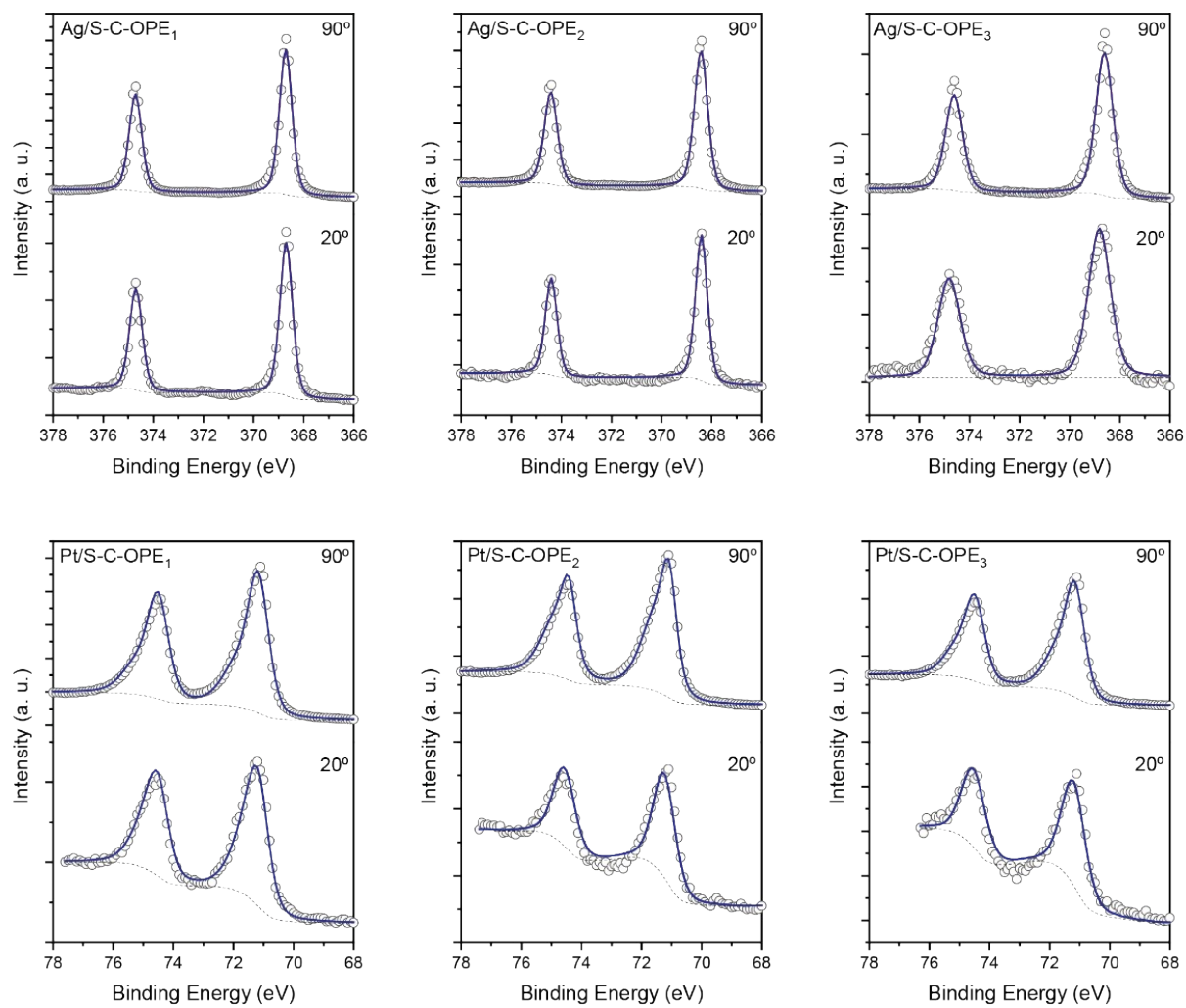
Figure S4. Ag $3d$ and Pt $4f$ spectra of SAMs Ag/S-CH$_2$-OPE$_n$Fc, and Pt/S-CH$_2$-OPE$_n$Fc ($n =$ 1−3) collected by 850 eV and 350 eV, respectively.

Table S1. Physical properties of SAMs Ag/S-CH$_2$-OPE$_n$Fc, Pt/S-CH$_2$-OPE$_n$Fc and Au/S-CH$_2$-OPE$_n$Fc (n = 1−3).

n	d_{SAM} (Å)[a,b]			α(°)[c]		
	Au	Pt	Ag	Au	Pt	Ag
n = 1	14.7 (13.6)	15.4 (13.1)	14.1 (12.9)	30	35	36
n = 2	21.6 (20.3)	19.9 (18.1)	20.0 (18.1)	25	37	37
n = 3	24.4 (25.5)	25.0 (23.6)	22.9 (23.9)	26	37	36

[a] The error for d_{SAM} is 2Å, estimated from 5% fitting error.

[b] Values in parentheses are calculated from the molecular length in the CPK model and the tilt angles α.

[c] α is the tilt angle of the Cp-OPE plane to the surface normal, derived from the NEXAFS signals of the peak I at the incident angle of 20° and 90°. The error is 5°, estimated from the linear fitting error of peak intensities against the incident angles.

S3. DFT calculation

Three DFT simulation cells were constructed to model the S-CH$_2$-OPE$_n$Fc (*n*=1-3) SAMs series on Au(111). We showed in earlier work that the positions and shapes of the high-lying valence and low-lying conduction band near-Fermi levels are not significantly affected by choice of M=Au, Ag or Pt.[4] The electronic structure calculations were carried out using density-functional theory (DFT) performed with the Vienna *ab initio* simulation package (VASP).[6] The models were described using periodic plane wave DFT with the GGA-PBE functional,[7] projector augmented wave (PAW)[8] pseudopotentials with a plane wave cut-off of 400 eV. The molecule-surface complexes were calculated under periodic boundary conditions with a 30 Å vacuum spacing in the direction normal to the four-layer gold surface. All atoms except the gold atoms in the bottom layer were allowed to relax unconstrained until the forces on each atom were <3 meV/Å. The conductance gaps E$_g$ were converged to below 100 meV for all SAMs using a 441 k-point grid.

The near-Fermi molecule-projected density of states (DOS) distributions of the S-CH$_2$-OPE$_n$Fc SAMs on Au(111) are shown in Fig. S5, together with the further decomposition into carbon atoms types in Fig. S6. The computed B, A, I, II and III electron density surfaces are shown in Fig. 2 in the text.
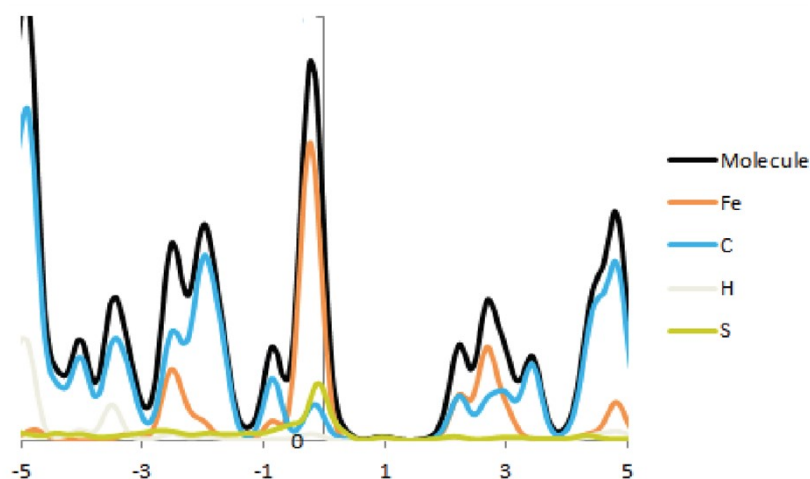
Figure S5. Calculated project density of states (PDOS) distributions for $Au/S\text{-}CH_2\text{-}OPE_1Fc$. All plots are centered on the Fermi level, which is shifted to 0.0 eV on the horizontal axis. The DOS population is given in arbitrary units on the vertical axis. Band energy ranges for the occupied A, B and unoccupied I, II, III levels identified by VB and NEXAFS are identified as B (HOMO-1): -3.0 → -1.0 eV; A (HOMO): -1.0 → 0.0 eV (Fermi level); I (LUMO): 1.8 → 2.4 eV; II (LUMO+1): 2.4 → 3.8 eV; III (LUMO+2): 3.8 → 5.0 eV.
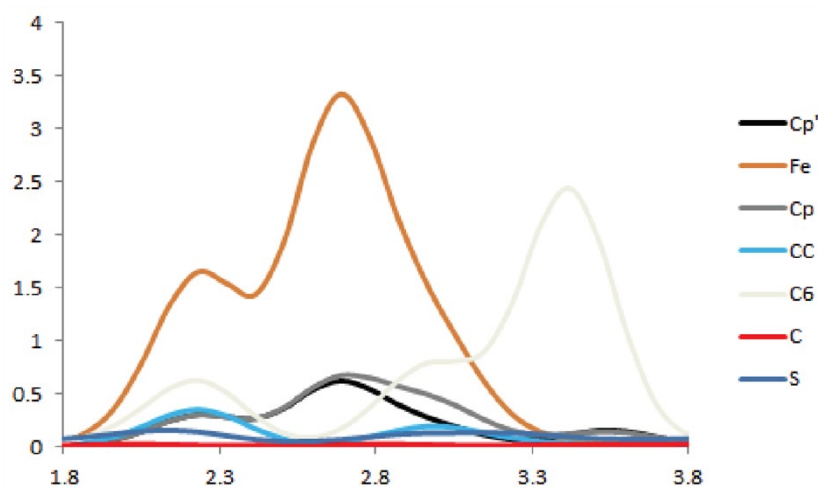

Figure S6. Calculated components to the PDOS in the regions I and II for $Au/S\text{-}CH_2\text{-}OPE_1Fc$, showing the iron, sulphur, and various carbon atom contributions. Cp' and Cp are cyclopentadienyl carbons above and below Fe, CC are C≡C carbons, C6 are phenyl Ph carbons, and C is the methylene CH_2 linker in the $Au/S\text{-}CH_2\text{-}OPE_nFc$ SAMs.

S4. Core-hole Clock analysis

We conducted the least-squares peak fitting for the RPES and NEXAFS spectra following a previously reported protocol.[4] Briefly, we obtained the intensity for each photon energy in RPES and NEXAFS spectra by integrating the valence band spectra in binding energy range of 0~7 eV and 0~20 eV, respectively. After subtracting the background, we proceeded to fit the peaks in RPES and NEXAFS while keeping the position and full width at half maximum for each component fixed. We treated the SAM of Au/S-OPE$_3$Fc as the isolated system where no charge transfer occurs between the Fc moieties and the metal substrates within the core-hole lifetime. The charge transfer time (τ_{CT}) for other systems can be derived from the relation[9]

$$\tau_{CT} = \tau_{CH} \frac{I_{\text{I-RPES}}^{\text{coup}} / I_{\text{I-NEXAFS}}^{\text{coup}}}{I_{\text{I-RPES}}^{\text{iso}} / I_{\text{I-NEXAFS}}^{\text{iso}} - I_{\text{I-RPES}}^{\text{coup}} / I_{\text{I-NEXAFS}}^{\text{coup}}} \qquad (S1)$$

in which τ_{CH} = 6 fs is the core-hole lifetime of C 1s, I^{iso} and I^{coup} represent the fitting area of resonance for the isolated Au/S-OPE$_3$Fc system and the studied coupled system. Figure S7 shows the fitting results for the NEXAFS spectra of the studied SAMs. Figure S8 displays the integrated RPES and NEXAFS spectra of Au/S-OPE$_3$Fc SAMs. The intensity ratio at each resonance represents the Iiso   I-RPES/Iiso   I-NEXAFS in Eq.(S1).
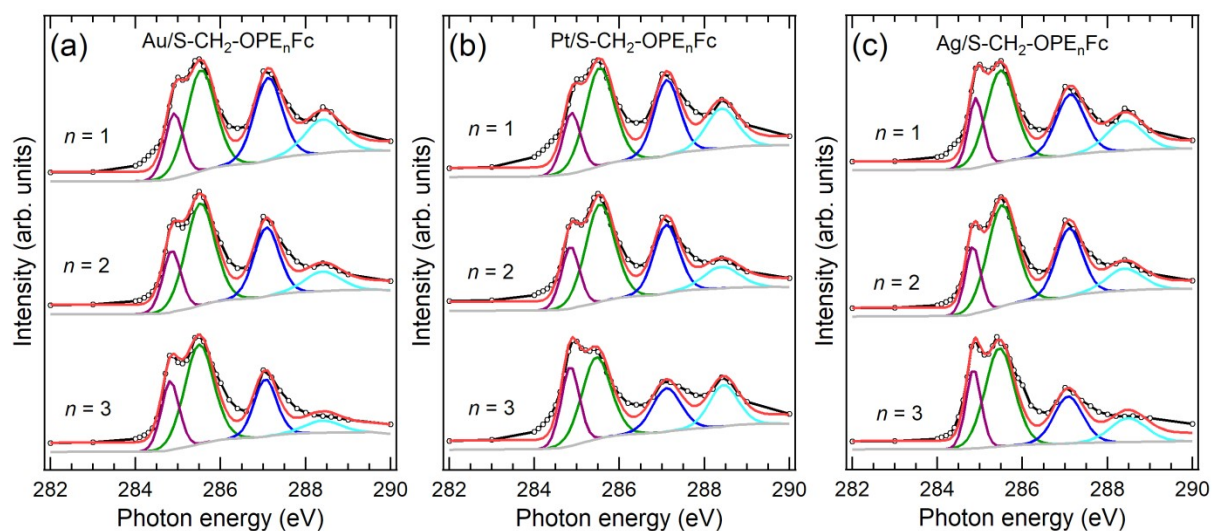
Figure S7. NEXAFS spectra for SAMs (a) Au/S-CH$_2$-OPE$_n$Fc, (b) Pt/S-CH$_2$-OPE$_1$Fc and (c) Ag/S-CH$_2$-OPE$_1$Fc (n = 1−3) and the corresponding fitting curves. The intensity for each photon energy is the integral of VB spectra from binding energy 0 eV to 20 eV. The fitted peak denotes resonance I (purple), II (green), III (blue) and IV (light green). The signals were all normalized by the NEXAFS spectra of corresponding clean metal surfaces to eliminate their impact on the peak intensity.
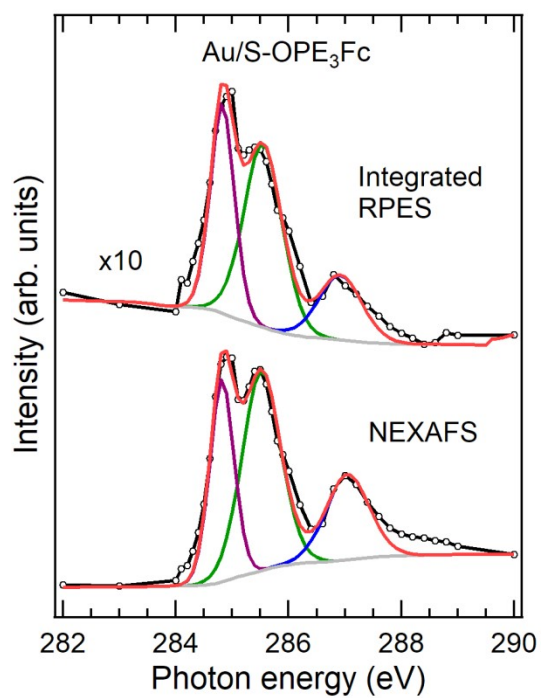
Fig. S8. Integrated RPES and NEXAFS spectra for SAMs of Au/S-OPE$_3$Fc, along with corresponding fitting curves. The RPES and NEXAFS intensities were obtained by integrating of VB spectra in the binding energy range of 0-7 eV and 0-20 eV, respectively.

S5. Junction fabrication and statistics

The junctions with cone-shaped tips of GaO_x/EGaIn as the top electrode were fabricated using previously reported procedures.[2] The bottom electrode was grounded using a copper wire and the top electrode of GaO_x/EGaIn was biased from $0\ V \rightarrow +1V \rightarrow 0\ V \rightarrow -1\ V \rightarrow 0\ V$. 360 to 460 traces were recorded for junctions based on each SAM which contained about 20 to 23 non-shorting junctions measured on 3 to 4 different substrates. The current density heatmaps for junctions $M/S-CH_2-OPE_nFc$ (M = Ag, Pt; $n = 1-3$) are shown in Figure S8 and Table S2 summarizes the statistics for these measurements. The $J(V)$ data and the junction statistics were reported before in ref.[10].
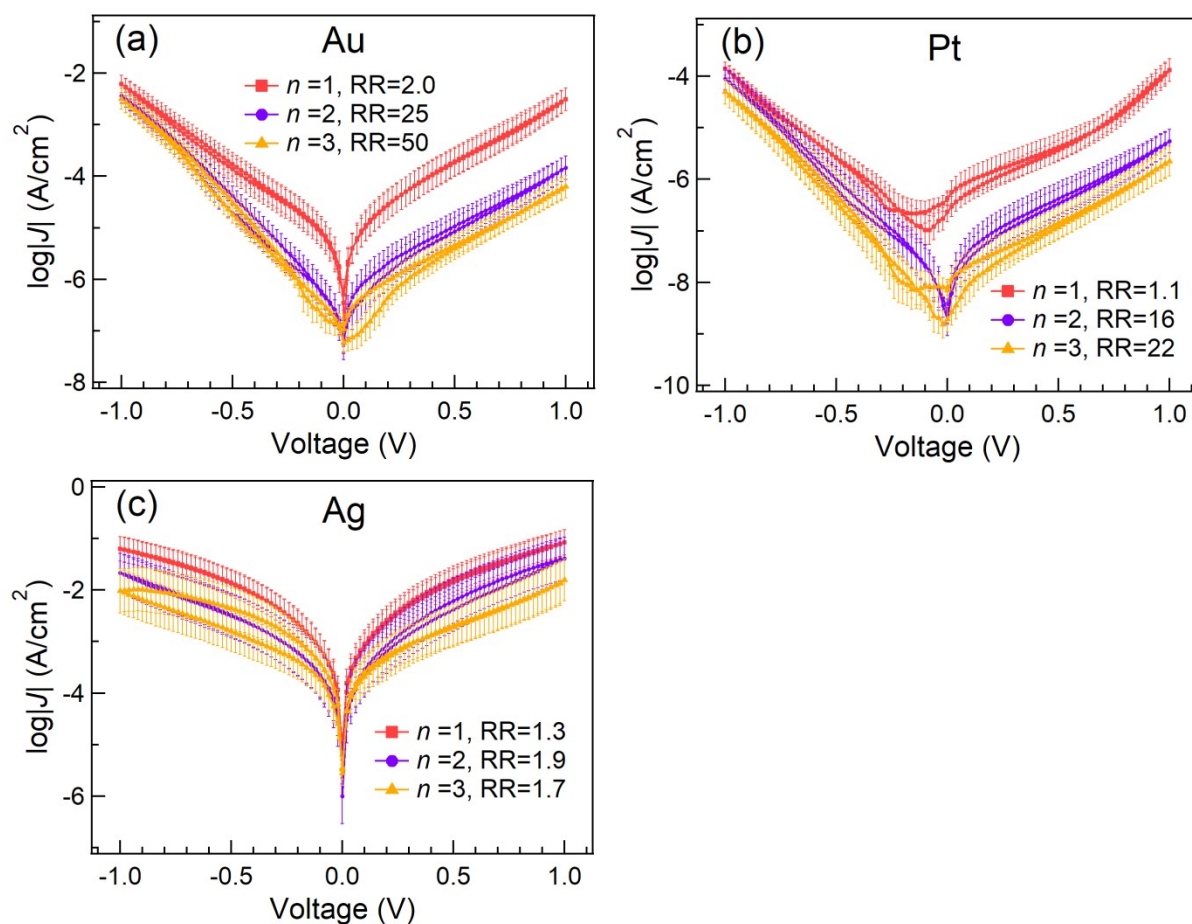

Figure S9. The values of $<\log_{10}|J|>_G$ as a function of V for (a) $Au/S-CH_2-OPE_nFc$ and (b) $Pt/S-CH_2-OPE_nFc$, and (c) $Ag/S-CH_2-OPE_nFc$ ($n = 1-3$). The error bars represent the 95% confidence intervals from 360-460 data points. Data for $Au/S-CH_2-OPE_nFc$ are taken from ref[10] for comparison.

Table S2. Junction statistics for the measurements conducted with cone-shaped EGaIn tips.

SAMs	No. of junctions	No. of traces	No. of shorts	Non-shorting junctions Yield (%)	Average log $|RR|$
Ag/S-CH$_2$-OPE$_1$Fc	20	400	4	83	0.11
Ag/S-CH$_2$-OPE$_2$Fc	20	400	2	91	0.28
Ag/S-CH$_2$-OPE$_3$Fc	20	400	3	87	0.23
Pt/S-CH$_2$-OPE$_1$Fc	20	460	1	95	0.04
Pt/S-CH$_2$-OPE$_2$Fc	21	420	0	100	1.20
Pt/S-CH$_2$-OPE$_3$Fc	18	360	0	100	1.34
Au/S-CH$_2$-OPE$_1$Fc	23	460	5	82	0.30
Au/S-CH$_2$-OPE$_2$Fc	23	460	6	79	1.40
Au/S-CH$_2$-OPE$_3$Fc	20	400	1	95	1.70

References

1. X. P. Chen, M. Roemer, L. Yuan, W. Du, D. Thompson, E. del Barco and C. A. Nijhuis, *Nat. Nano.*, 2017, **12**, 797-803.

2. Y. M. Han, C. Nickle, Z. Y. Zhang, H. Astier, T. J. Duffin, D. C. Qi, Z. Wang, E. del Barco, D. Thompson and C. A. Nijhuis, *Nat. Mater.*, 2020, **19**, 843-848.

3. L. Yuan, R. Breuer, L. Jiang, M. Schmittel and C. A. Nijhuis, *Nano Lett.*, 2015, **15**, 5506-5512.

4. Z. Y. Zhang, L. Cao, X. Chen, D. Thompson, D. C. Qi and C. A. Nijhuis, *J. Phys. Chem. C*, 2021, **125**, 18474-18482.

5. John F. Moulder, William F. Stickle, Peter E. Sobol and K. D. Bomben, *Handbook of X Ray Photoelectron Spectroscopy: A Reference Book of Standard Spectra for Identification and Interpretation of XPS Data*, Physical Electronics, 1995.

6. G. Kresse and J. Hafner, *Phys. Rev. B*, 1994, **49**, 14251-14269.

7. J. P. Perdew, K. Burke and M. Ernzerhof, *Phys. Rev. Lett.*, 1996, **77**, 3865-3868.

8. P. E. Blöchl, *Phys. Rev. B*, 1994, **50**, 17953-17979.

9. P. A. Brühwiler, O. Karis and N. Mårtensson, *Rev. Mod. Phys.*, 2002, **74**, 703-740.

10. C. A. Nijhuis, Z. Zhang, F. Adoah, C. Nickle, S. K. Karuppannan, L. Wang, L. Jiang, A. Tadich, B. Cowie, T. Salim, D.-C. Qi, D. Thompson and E. D. Barco, *Adv. Electron. Mater.*, 2023, **9**, 2200637.